

# Effects of Catalyst Phase on the Hydrogen Evolution Reaction of Water Splitting: Preparation of Phase-Pure Films of FeP, Fe<sub>2</sub>P, and Fe<sub>3</sub>P and Their Relative Catalytic Activities

Desmond E. Schipper,<sup>†,⊥</sup> Zhenhuan Zhao,<sup>‡,||,⊥</sup> Hari Thirumalai,<sup>§</sup> Andrew P. Leitner,<sup>†</sup> Samantha L. Donaldson,<sup>†</sup> Arvind Kumar,<sup>†</sup> Fan Qin,<sup>‡,||</sup> Zhiming Wang,<sup>||</sup> Lars C. Grabow,<sup>\*,§,Ⓢ</sup> Jiming Bao,<sup>\*,‡,||</sup> and Kenton H. Whitmire<sup>\*,†,Ⓢ</sup>

<sup>†</sup>Department of Chemistry, Rice University, Houston, Texas 77005, United States

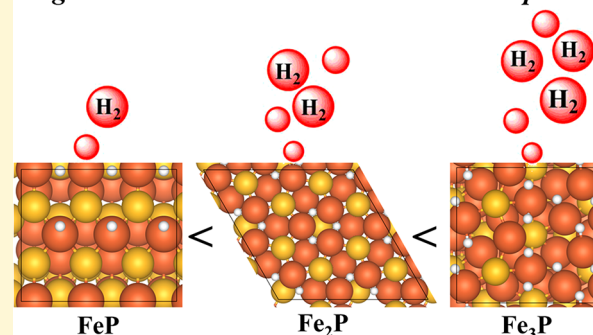
<sup>‡</sup>Department of Electrical and Computer Engineering and <sup>§</sup>Department of Chemical and Biomolecular Engineering, University of Houston, Houston, Texas 77204, United States

<sup>||</sup>Institute of Fundamental and Frontier Sciences, University of Electronic Science and Technology of China, Chengdu 610054, China

## Supporting Information

**ABSTRACT:** The comparative catalytic activities of iron phosphides, Fe<sub>x</sub>P (*x* = 1–3), have been established with phase-pure material grown by chemical vapor deposition (CVD) from single-source organometallic precursors. This is the first report of the preparation of phase-pure thin films of FeP and Fe<sub>2</sub>P, and their identity was established with scanning-electron microscopy, X-ray photoelectron spectroscopy, and powder X-ray diffraction. All materials were deposited on fluorine-doped tin oxide (FTO) for evaluation of their activities toward the hydrogen evolution reaction (HER) of water splitting in 0.5 M H<sub>2</sub>SO<sub>4</sub>. HER activity follows the trend Fe<sub>3</sub>P > Fe<sub>2</sub>P > FeP, with Fe<sub>3</sub>P having the lowest overpotential of 49 mV at a current density of 10 mA cm<sup>-2</sup>. Density functional theory (DFT) calculations are congruent with the observed activity trend with hydrogen binding favoring the iron-rich terminating surfaces of Fe<sub>3</sub>P and Fe<sub>2</sub>P over the iron-poor terminating surfaces of FeP. The results present a clear trend of activity with iron-rich phosphide phases outperforming phosphorus rich phases for hydrogen evolution. The films of Fe<sub>2</sub>P were grown using Fe(CO)<sub>4</sub>PH<sub>3</sub> (1), while the films of FeP were prepared using either Fe(CO)<sub>4</sub>P<sup>t</sup>BuH<sub>2</sub> (2) or the new molecule {Fe(CO)<sub>4</sub>P(H)<sup>t</sup>Bu}<sub>2</sub> (3) on quartz and FTO. Compound 3 was prepared from the reaction of PCl<sub>2</sub><sup>t</sup>Bu with a mixture of Na[HF<sub>2</sub>(CO)<sub>4</sub>] and Na<sub>2</sub>[Fe(CO)<sub>4</sub>] and characterized by single-crystal X-ray diffraction, ESI-MS, elemental analysis, and <sup>31</sup>P/<sup>1</sup>H NMR spectroscopies. Films of Fe<sub>3</sub>P were prepared as previously described from H<sub>2</sub>Fe<sub>3</sub>(CO)<sub>9</sub>P<sup>t</sup>Bu (4).

## Single-Source Precursor Derived Iron Phosphides



## INTRODUCTION

As a consequence of the extraordinary richness of the phase-space of the transition-metal phosphides (TMPs),<sup>1</sup> a number of desirable, phase-dependent properties can be obtained from combinatory mixtures of as few as two elements. The iron–phosphorus system possesses six known phases: Fe<sub>4</sub>P, Fe<sub>3</sub>P, Fe<sub>2</sub>P, FeP, FeP<sub>2</sub>, and FeP<sub>4</sub>, whose compositional and structural differences lead to varying electronic and physicochemical properties.<sup>2</sup> For example, increasing the amount of phosphorus from Fe<sub>3</sub>P through FeP<sub>4</sub> takes the material from a high temperature ferromagnet to a semiconductor.<sup>3,4</sup> Hexagonal Fe<sub>2</sub>P is known to exhibit the magnetocaloric effect with a magnetic entropy change ( $\Delta S_m$ ) of 2.7 J·kg<sup>-1</sup> for a 2 T field change,<sup>5</sup> and its magnetocaloric effect becomes “giant” when doped with manganese and arsenic ( $\Delta S_m = 14.5$  J·kg<sup>-1</sup> for a 2 T field change).<sup>6</sup> Furthermore, FeP and FeP<sub>2</sub> have been

demonstrated to be high-performance anode materials for lithium-ion batteries.<sup>7,8</sup>

More recently, the catalytic properties of the TMPs have become the object of intense study. First recognized for their hydroprocessing abilities,<sup>9</sup> TMPs gained eminence as water-splitting catalysts following the report of FeP nanosheets catalyzing the hydrogen evolution reaction (HER) efficiently.<sup>10</sup> Since then, most binary and ternary TMPs of the catalytically active metals have been evaluated for the HER and even the oxygen evolution reaction (OER), including several reports concerning the iron phosphides.<sup>11–17</sup> Several syntheses of FeP and Fe<sub>2</sub>P nanostructures using thermal phosphidation of metals or metal oxides and their performance toward the HER have

Received: April 18, 2018

Revised: April 26, 2018

Published: April 26, 2018

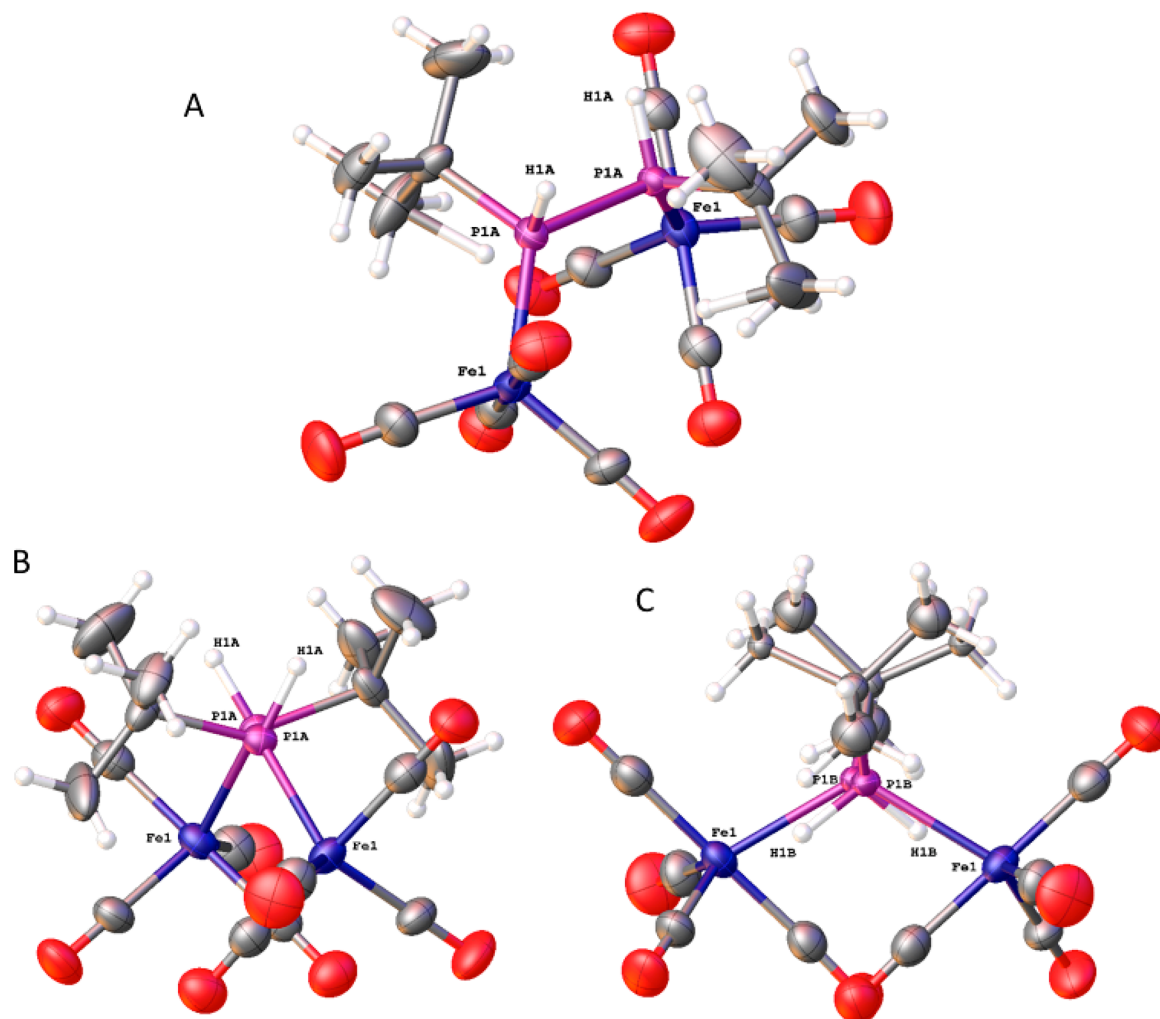
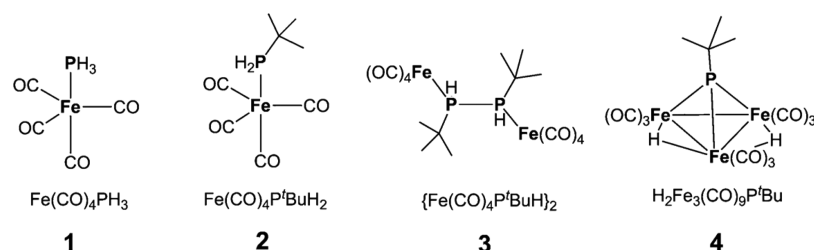


**Figure 1.** (A) Crystal structure of the major component of 3 (R,R isomer). (B) Major component of 3 viewed down the P–P bond. (C) Minor component of 3 viewed down the P–P bond. Thermal ellipsoids are given at 50% probability.

been reported.<sup>11,18,19</sup> These methods, however, require high temperatures and hazardous phosphines and drastically limit the substrates on which the metal phosphides can be grown.<sup>15–17</sup> Additionally, phase and compositional purity is difficult to ensure by these methods. These considerations limit utilization of these materials as water-splitting catalysts and in other applications and make accurate determination of properties, including catalytic activities, of so-produced metal phosphides difficult or impossible.

We have recently shown that metal–organic chemical vapor deposition using single-source molecular precursors (SS-MOCVD) has been a fruitful means to achieving thin films of binary and ternary TMPs.<sup>20–22</sup> The method relies on the ability to control the stoichiometry of the produced materials by building the desired stoichiometry into the precursor. In this way, Fe<sub>3</sub>P and FeMnP thin films on quartz have been obtained

using H<sub>2</sub>Fe<sub>3</sub>(CO)<sub>9</sub>P<sup>t</sup>Bu and FeMn(CO)<sub>8</sub>(μ-PH<sub>2</sub>) as precursors.<sup>21,22</sup> The method was extended to afford additional compositional variation by codecomposing isostructural precursors with varying stoichiometry. This yielded (Fe<sub>1–x</sub>Co<sub>x</sub>)<sub>3</sub>P in the range (0.09 < x < 0.22), which was synthesized by employing blends of H<sub>2</sub>Fe<sub>3</sub>(CO)<sub>9</sub>P<sup>t</sup>Bu and Co<sub>3</sub>(CO)<sub>9</sub>P<sup>t</sup>Bu as the MOCVD feedstock.<sup>20</sup> Among the key advantages of the SS-MOCVD method are the ability to grow complex, single-phase TMPs directly on active substrates nondestructively and without the use of binders. For example, the growth of FeMnP on a TiO<sub>2</sub>-nanorod array yielded a highly active photoanode while FeMnP grown on conductive, three-dimensional nickel foam serves as an electrode for both water-splitting half-reactions, with state-of-the-art performance obtained from a tandem cell configuration.<sup>23</sup>

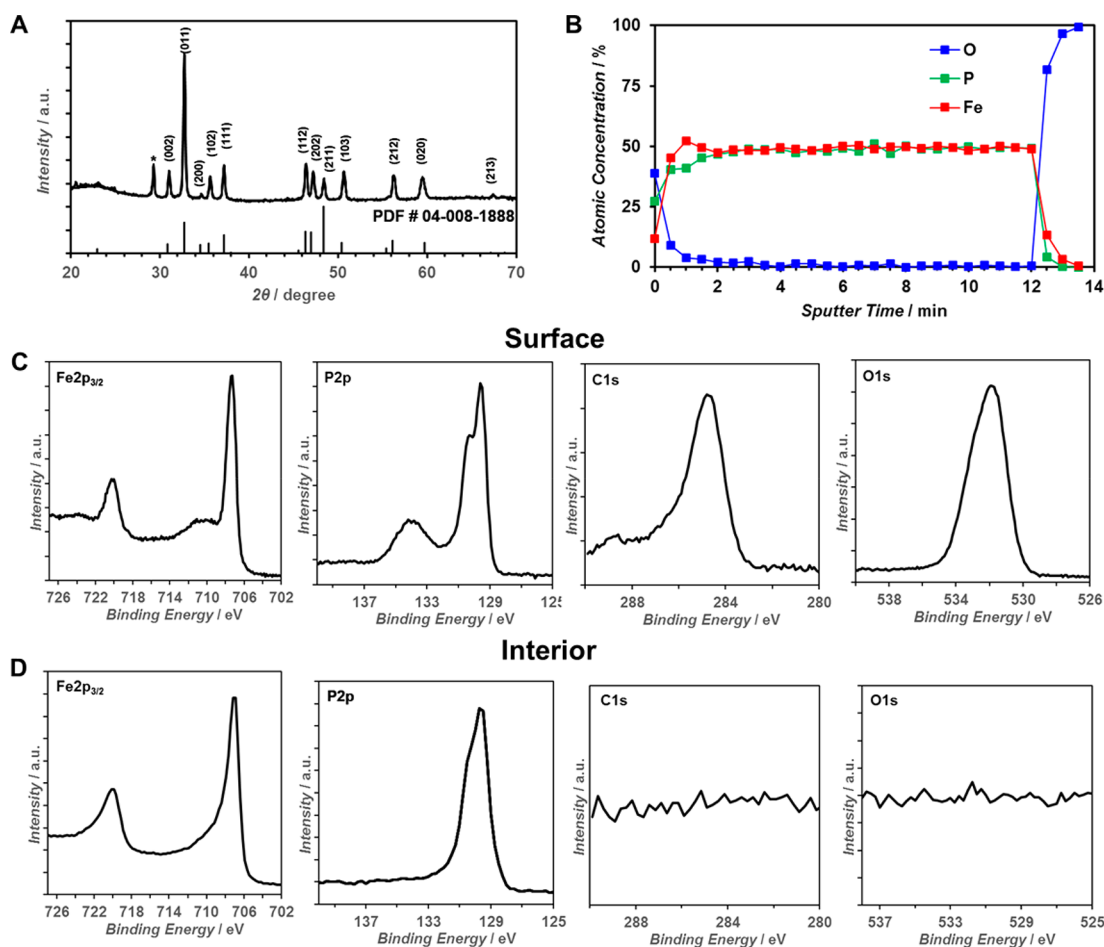
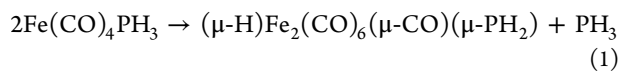


**Figure 2.** XRD, XPS, and XPS depth profile of FeP on quartz. (A) XRD, (B) XPS depth profile, (C) surface XPS spectra, and (D) interior XPS spectra. Peaks denoted by \* in the XRD pattern arise from the substrate.

## RESULTS AND DISCUSSION

**MOCVD Growth of Phase Pure Thin Films of FeP and Fe<sub>2</sub>P.** The SS-MOCVD method previously developed for the growth of Fe<sub>3</sub>P has been applied to production of thin films of FeP and Fe<sub>2</sub>P on quartz and FTO (Figure S1).

Compound **1** has been previously demonstrated to yield nanoparticles of FeP by solution-based decomposition<sup>24</sup> and was explored as a CVD precursor; however, it was found that Fe<sub>2</sub>P was the only material that deposited on a quartz substrate in our apparatus at 350 °C (Table S1). The <sup>31</sup>P and <sup>1</sup>H NMR spectra of the off-gases from the decomposition of **1** under CVD conditions confirmed the elimination of PH<sub>3</sub> (Figures S2–S5). At temperatures ≥ 400 °C, a mixture of FeP and Fe<sub>2</sub>P was obtained. The ability to form phase pure Fe<sub>2</sub>P suggests that there is a very clean rearrangement process occurring at the lower temperatures to give a precise Fe<sub>2</sub>P precursor with stoichiometric loss of P. A possible intermediate step is provided in eq 1.



It was reasoned that with Compound **2**, a <sup>t</sup>Bu group in place of a hydrogen could slow, and potentially stop, the release of phosphorus as PH<sub>3</sub> during decomposition since PH<sub>2</sub><sup>t</sup>Bu is a stronger donor and should be bound more tightly.<sup>25</sup> At 350 °C, Fe<sub>2</sub>P was again the product but decomposition of **2** at 450 °C gave phase-pure FeP. Although both **1** and **2** lost phosphorus at

350 °C, the loss of phosphorus from **1** was slowed by increasing the decomposition temperature to 450 °C and eliminated completely using **2** at 450 °C, suggesting that decomposition occurs at that temperature before rearrangement with the loss of phosphorus can take place.

While both precursors gave Fe<sub>2</sub>P as the sole product at lower decomposition temperatures (350 °C), more crystalline Fe<sub>2</sub>P was obtained from **1**. In contrast, the new derivative **3** that contains a P–P bond was found to give pure FeP at 350 °C, although the deposition time required (8 h vs 15 m) was longer due to the lower volatility of **3** compared to that of **2**. The films of FeP derived from **2** or **3**, however, were indistinguishable.

Compound **3**, which is a rare example of metalated organodiphosphane, is prepared by treating an equal molar mixture of Na[HF<sub>2</sub>(CO<sub>4</sub>)] and Na<sub>2</sub>[Fe(CO)<sub>4</sub>] with <sup>t</sup>BuPCl<sub>2</sub> in tetrahydrofuran (see Experimental Details, SI). The molecule crystallizes in the chiral space group *P*<sub>4</sub><sub>3</sub><sub>2</sub><sub>1</sub><sub>2</sub> as a racemic twin (Figure 1) possessing two crystallographically distinct, dimeric “Fe(CO)<sub>4</sub>(H)P<sup>t</sup>Bu” units joined by a P–P bond. The diphosphine (P<sup>t</sup>BuH)<sub>2</sub> has never before been observed as a ligand, and only six examples of a diphosphine with formula = [PR(H)]<sub>2</sub> have been previously structurally characterized.<sup>26–30</sup> Notably, the diphosphane coordinates at the equatorial rather than axial positions on Fe, an uncommon configuration usually associated with π-acceptor ligands.<sup>31,32</sup> The molecule is C<sub>2</sub> symmetric, and both enantiomers are observed in an 85:15 ratio in the structure, although the crystals themselves are chiral

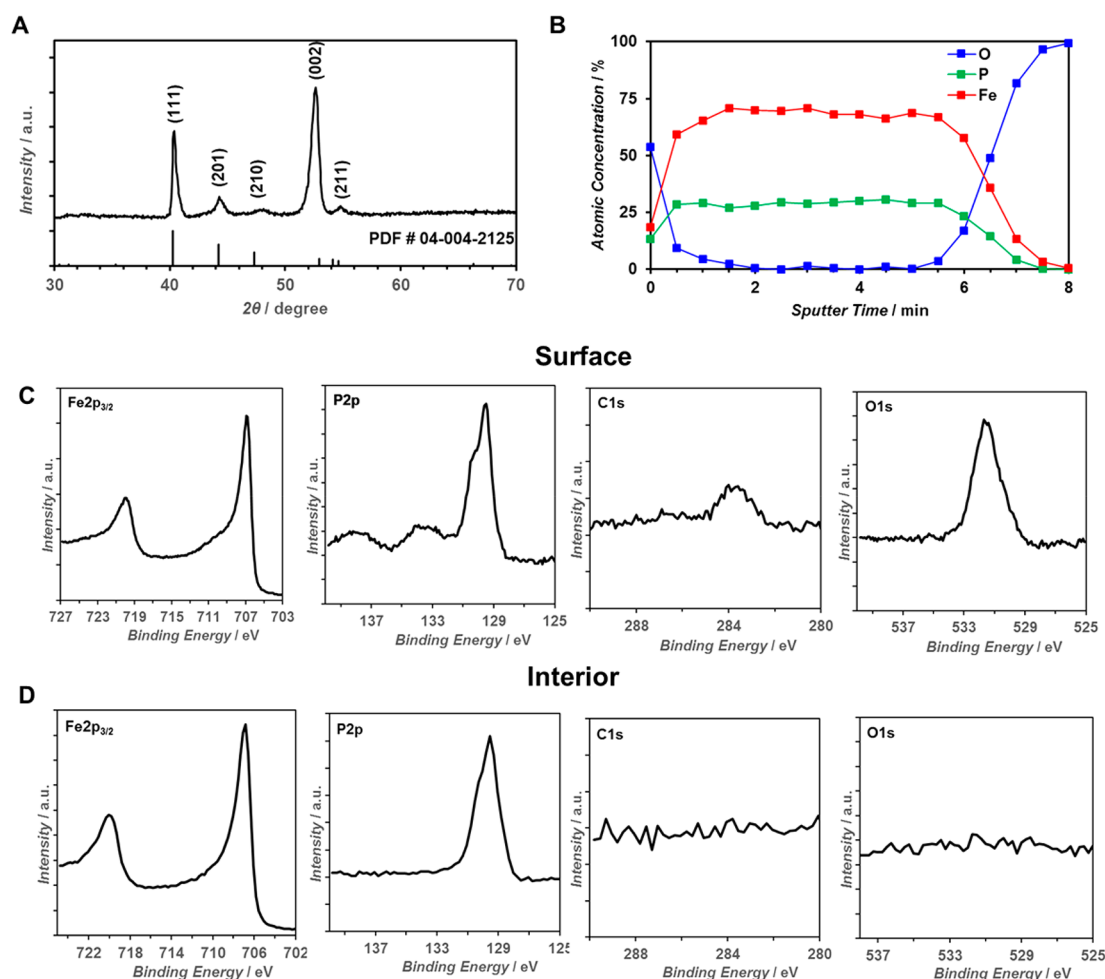


**Figure 3.** XRD, XPS, and XPS depth profile of  $\text{Fe}_2\text{P}$  on quartz. (A) XRD, (B) XPS depth profile, (C) surface XPS spectra, and (D) interior XPS spectra.

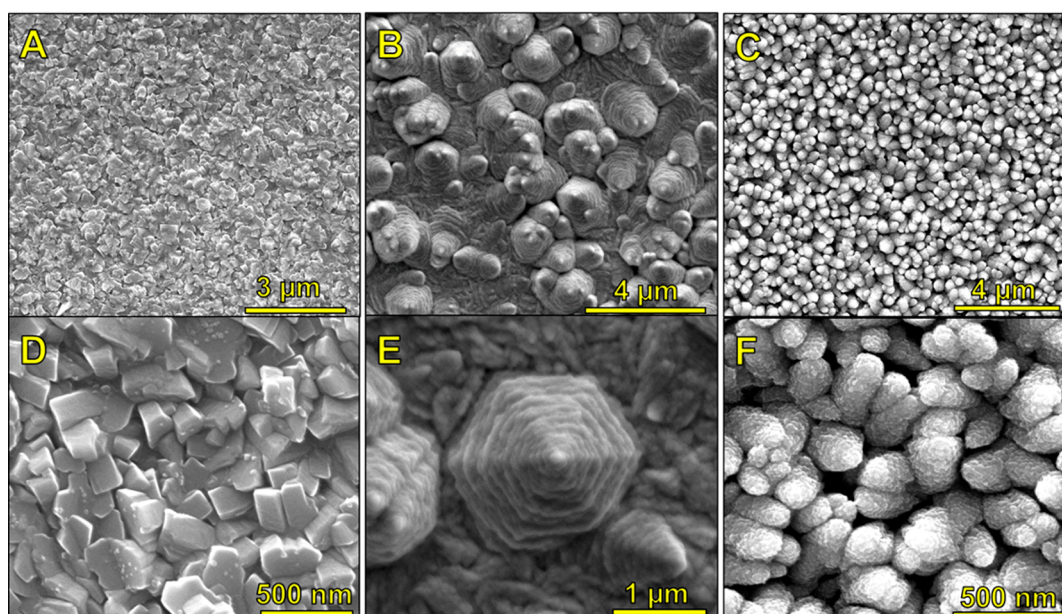


**Figure 4.** SEM images of  $\text{FeP}$  (A and D),  $\text{Fe}_2\text{P}$  (B and E), and  $\text{Fe}_3\text{P}$  (C and F) on FTO.

and refined as a racemic twin. Interestingly the two forms in the crystal structure show dramatically different rotational conformations (Figure 1). The  $^{31}\text{P}$  and  $^1\text{H}$  NMR spectra (Figures

S6–S12) show complex second order behavior with the overall pattern consistent with those observed for the few existing related compounds.<sup>27,28</sup> The negative ion ESI-MS shows the

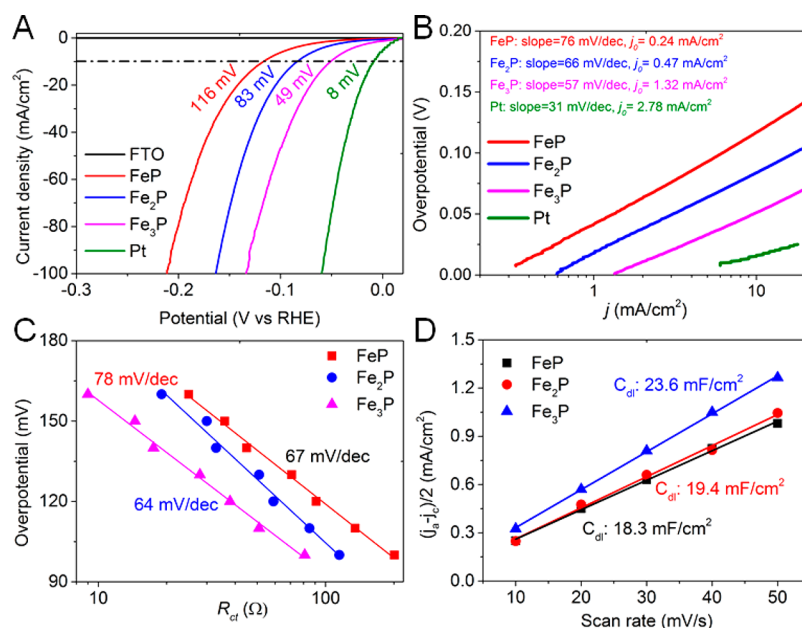


**Figure 5.** Electrochemical characterization. (A) Polarization curves. (B) Corresponding Tafel slopes. (C) Charge transfer Tafel slopes. (D) Half of the current density differences as a function of scan rate. The  $C_{dl}$ , the electrochemical double-layer capacitance, is the slope of the fitted line.

[P–H<sup>+</sup>]<sup>–</sup> ion very cleanly with successive loss of five CO ligands (Figures S13–S15). Crystallographic refinement parameters and selected bond lengths and angles are available in Tables S2 and S3 in the SI.

**Film Characterization.** The films on quartz were characterized by (1) X-ray photoelectron spectroscopy (XPS) depth-profiling to ascertain homogeneity and (2) scanning electron microscopy (SEM) for morphology (Figures S16–S19) and (3) powder-X-ray diffraction (PXRD) to establish phase (Figures S20–S25). The powder pattern of FeP was indexed to its known orthorhombic *Pnma* setting (Figure 2a). XPS depth profiling confirmed a 1:1 Fe:P ratio with only trace oxygen and carbon (Figure 2d). The surface was partially oxidized, but the interior was composed solely of Fe and P whose binding energies of 706.9 and 129.65 eV closely match the literature values of 706.9 and 129.34 eV, respectively.<sup>33</sup> The SEM images show that the film consists of rectangular crystallites approximately 500 nm in length (Figure S17). Films of FeP on quartz from precursor 3 were morphologically similar (Figure S18), although preferred orientation is apparent in the powder spectrum (Figure S20).

Similarly, Fe<sub>2</sub>P was characterized by SEM (Figure S19), PXRD (Figure 3a), and XPS analysis with depth profiling (Figure 3b–d). The XRD pattern was indexed to the known hexagonal *P62m* setting for Fe<sub>2</sub>P. XPS depth profiling demonstrated the film is homogeneous with only trace oxygen and carbon. Like the FeP, the surface was partially oxidized, but the interior was pristine. The binding energies for Fe and P were 706.8 and 129.55 eV, close to the reported values of 706.8 and 129.31 eV.<sup>33</sup> SEM shows the film to consist of contiguous hexagonal towers, reflecting the hexagonal symmetry of the Fe<sub>2</sub>P crystal system.

The film containing an FeP/Fe<sub>2</sub>P mixture produced from the decomposition of 1 at 450 °C was characterized by SEM (Figure S16) and PXRD (Figure S21) and is composed of large, poorly defined crystallites.

FeP, Fe<sub>2</sub>P, and Fe<sub>3</sub>P were grown on FTO analogously to the depositions on quartz. Fe<sub>3</sub>P was grown as previously

reported.<sup>21</sup> The films were characterized by XRD, SEM, and XPS. The XRD patterns of the respective materials confirm the phase identity and purity of the respective iron phosphides (Figures S22–S25). SEM images reveal clear morphological differences among the iron phosphides (Figure 4).

FeP consists of rectangular prisms, Fe<sub>2</sub>P stacked hexagonal sheets, and Fe<sub>3</sub>P cauliflower-like growths. These shapes can be attributed to the crystal structures of the respective iron phosphides. The rectangular blocks observed for FeP are consistent with an orthorhombic space group, the hexagonal sheets observed for Fe<sub>2</sub>P are consistent with a hexagonal space group, and the cauliflower-like shape for the Fe<sub>3</sub>P can be attributed to its tetragonal crystal system which has a tendency to twin along the {011} faces.

**Catalytic Activity of the Iron Phosphide Films.** For HER characterization, films of FeP, Fe<sub>2</sub>P, and Fe<sub>3</sub>P, whose synthesis on quartz has been detailed previously starting from H<sub>2</sub>Fe<sub>3</sub>(CO)<sub>9</sub>P<sup>t</sup>Bu (4), were grown on FTO. Importantly, the ability to use a single method to grow films of phase-pure, high quality (trace oxygen and carbon) materials cleanly on a conductive substrate facilitates direct comparison of FeP, Fe<sub>2</sub>P, and Fe<sub>3</sub>P. It is shown that the sequence of HER activity follows the series Fe<sub>3</sub>P > Fe<sub>2</sub>P > FeP with stability following the same trend. These results point to metal-rich phosphides, particularly the Fe<sub>3</sub>P phase, as being superior to metal-poor phosphides for HER.

The HER activity was evaluated with a three-electrode configuration in 0.5 M H<sub>2</sub>SO<sub>4</sub>, and the respective as-deposited iron phosphide on FTO was directly used as the working electrode. Figure 5A,B shows the polarization curves after *iR*-correction and the corresponding Tafel slopes for the iron phosphides. The overpotential is defined as the potential to reach a current density of 10 mA/cm<sup>2</sup>.<sup>34</sup> The performance of Pt was used as a reference and is in good agreement with reported values;<sup>35</sup> the bare FTO shows negligible HER performance. The overpotentials for the FeP, Fe<sub>2</sub>P, and Fe<sub>3</sub>P electrodes are 116 mV, 83 mV, and 49 mV, respectively, as shown in Figure 5A. The corresponding Tafel slopes for FeP, Fe<sub>2</sub>P, and Fe<sub>3</sub>P are

79 mV/dec, 66 mV/dec, and 57 mV/dec. The HER performance increases in the order FeP, Fe<sub>2</sub>P, and Fe<sub>3</sub>P, with the increase of iron content or with the decrease of P content. The exchange current density ( $j_0$ ) was obtained by extrapolating the linear part of the Tafel plots to intersect with the  $x$ -axis.<sup>36</sup> Fe<sub>3</sub>P has the highest intrinsic catalytic activity of the tested iron phosphides as assessed by having the highest exchange current density of 1.32 mA/cm<sup>2</sup> as shown in Figure 5B.

Nyquist plots derived from electrochemical impedance spectroscopy (EIS) were employed to investigate the HER kinetics, as shown in Figure S26. All electrodes show a similar semicircular profile without Warburg impedance in the low frequency range, indicating the mass transport is rapid and is kinetically controlled.<sup>37</sup> The active sites at the surface can be easily accessed by the electrolyte ions. The Nyquist plots can be fitted with the equivalent circuit consisting of the equivalent series resistance ( $R_s$ ) and the charge transfer resistance ( $R_{ct}$ ) with the constant element referring to the double layer capacitance. All the electrodes have similar  $R_s$  values of about 5  $\Omega$ . Fe<sub>3</sub>P exhibits the lowest charge transfer resistance of 25  $\Omega$  at the same overpotential of 160 mV, compared to FeP and Fe<sub>2</sub>P, indicating that Fe<sub>3</sub>P has the fastest charge transfer rate during the HER.<sup>38</sup> The charge transfer Tafel slope was determined from the slope of the linear fitting of the plot of  $\log R_{ct}$  versus overpotential (Figures 5C and S27). It is found that the values of the slopes fall between 39 mV/dec and 118 mV/dec, indicating the charge transfer is the rate-determining step.<sup>39</sup> The Fe<sub>3</sub>P electrode displays the lowest charge transfer Tafel slope of 64 mV/dec, further confirming that its charge transfer kinetics in the HER process are faster than those of Fe<sub>2</sub>P and FeP.

The electrocatalytically active surface area (ECSA) was obtained by measuring the electrochemical double layer capacitance using cyclic voltammetry in a non-Faradaic reaction potential range, as shown in Figure S28 and Figure 5D. The ECSAs for FeP, Fe<sub>2</sub>P, and Fe<sub>3</sub>P were 18.3 mF/cm<sup>2</sup>, 19.4 mF/cm<sup>2</sup>, and 23.6 mF/cm<sup>2</sup>, respectively. The Fe<sub>3</sub>P possesses the largest ECSA, in good agreement with it exhibiting the highest HER performance.

We also investigated the long-term stability of the as-deposited catalysts by chronoamperometry measurements at an overpotential of 120 mV in 0.5 M H<sub>2</sub>SO<sub>4</sub> solution (Figure S29A). The current density of Fe<sub>3</sub>P is almost 2.7 times higher and six times higher than those of Fe<sub>2</sub>P and FeP, respectively, further confirming the superior HER performance of Fe<sub>3</sub>P compared to Fe<sub>2</sub>P and FeP. All the electrodes show stable current density over 20 h of operation. The Faradaic efficiencies of FeP, Fe<sub>2</sub>P, and Fe<sub>3</sub>P were evaluated by comparing the measured amount of hydrogen by gas chromatography to the calculated amount of hydrogen according to the recorded current. The Faradaic efficiencies were 96%, 98%, and 97% for FeP, Fe<sub>2</sub>P, and Fe<sub>3</sub>P (Figure S29B), respectively.

The oxidation states of the tested Fe<sub>3</sub>P film were determined with XPS (Figure S30). The surface XPS spectra indicate the existence of Fe and P consistent with an iron phosphide having peaks located at 707.6 eV for Fe and 129.4 eV for P. That both Fe and P were found at the surface following testing in their zerovalent state is consistent with catalysis of HER by the iron phosphide. Furthermore, we found that there was no detectable Pt at the surface of the tested Fe<sub>3</sub>P sample. In order to eliminate this potential source of contamination,<sup>40,41</sup> we conducted cyclic voltammetry at a scan rate of 100 mV/s for

600 cycles using Pt and a graphite rod as the counter electrode, respectively, as shown in Figure S31. It was found that the profiles of the polarization curves are very close to each other. Compared to the first cycle, the curves at the 600<sup>th</sup> cycle shift to more negative potentials for the Pt and graphite rod counter electrodes. Therefore, we can safely conclude that there is no Pt contamination of the working electrode.

In this study, we have precise control over the stoichiometry of the iron and phosphorus content, and the catalysts are deposited onto planar FTO substrates to form uniform thin films, meaning that the FTO substrate has less effect on the geometric current density than common 3D substrates like Cu foam and Ni foam. The normalized current density by ECSA in Figure S32 indicates that the HER activity obeys the order of Fe<sub>3</sub>P > Fe<sub>2</sub>P > FeP. The as-deposited Fe<sub>3</sub>P on FTO shows better than, or comparable, HER performance to Fe<sub>2</sub>P and FeP in acidic media. Table S4 summarizes the HER performance of recently developed transition metal phosphides for comparison.

**Insights from Density Functional Theory (DFT) Calculations.** The role of phosphorus in hydrogen evolution by TMPs has remained poorly understood but is of immediate importance given the number of M<sub>x</sub>P<sub>y</sub> phases available for any given metal (M). Furthermore, the question of how much phosphorus is optimal for the HER process is unresolved. Previous theoretical studies have suggested that transition metal atoms function as the catalytic reaction centers with the negatively charged and weakly basic P atoms assisting in trapping protons and promoting the desorption of H<sub>2</sub>.<sup>16,36,42</sup> However, among literature reports, there is no clear trend in activities for the hitherto tested iron phosphides, namely, FeP<sub>2</sub>, FeP, and Fe<sub>2</sub>P. As summarized in Table S4, the overpotentials of reported FeP nanostructures range from from 31 mV to 154 mV for 10 mA/cm<sup>2</sup> of current density ( $j$ ),<sup>11,43–47</sup> while the corresponding overpotentials of Fe<sub>2</sub>P nanostructures range from 88 mV to 191 mV.<sup>18,48,49</sup> The single report on FeP<sub>2</sub> as an HER electrocatalyst provides an overpotential value ( $j = 10$  mA/cm<sup>2</sup>) of 61 mV, more in the range of FeP.<sup>47</sup> The large variations, even for a given phase, likely stem from differences in electrode fabrication methods, the types of nanostructures (e.g., nanoparticles vs nanowires), the presence or lack of surface stabilizing agents, and the phase inhomogeneities which can be expected for the types of preparatory methods. Although previous reports of iron phosphide HER activities are unresponsive of a trend, more convincing trends can perhaps be accepted for Mo, Co, and Ni phosphides for which it was found that metal-poor phases outperformed metal-rich phases.<sup>36</sup> Conversely, Rappe and co-workers proposed that Ni<sub>3</sub>P surfaces are better HER catalysts than Ni<sub>2</sub>P surfaces although worse than Ni<sub>5</sub>P<sub>4</sub> surfaces, based on a series of detailed DFT calculations and thermodynamic considerations of the active surface at typical reaction conditions.<sup>50,51</sup> While this recent experimental and theoretical study adds some uncertainty to the generality of established activity trends among Ni phosphides, we provide experimental evidence for increasing HER activity with decreasing P content for Fe phosphides.

To further support our experimental observation and to gain additional understanding of the electrocatalytic activity among iron phosphides, we performed a series of DFT calculations to understand the hydrogen binding preferences on select surface facets predicted by the Bravais–Friedel–Donnay–Harker (BFDH) crystal morphology algorithm.<sup>52</sup> The full simulation details are provided in the SI (see Density Functional Theory

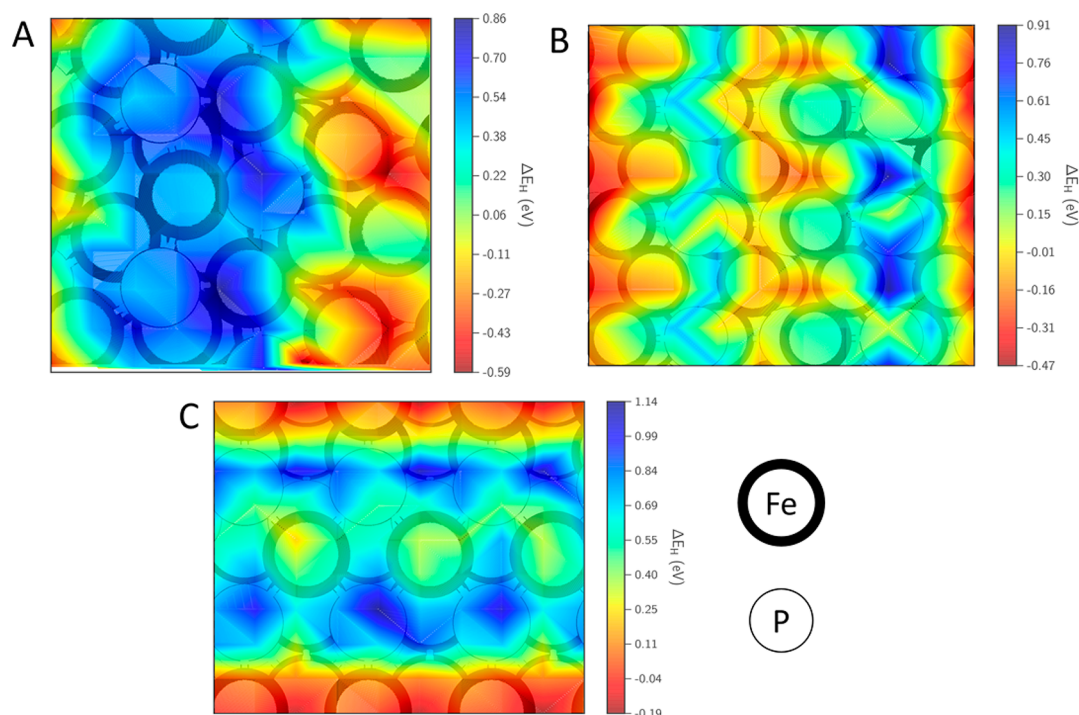


**Figure 6.** Contours of H binding strength on the surfaces of (a)  $\text{Fe}_3\text{P}$  (100); (b)  $\text{Fe}_2\text{P}$  (100); and (c)  $\text{FeP}_{\text{Fe-t}}$  (011). Fe atoms are depicted with thick boundaries, while P atoms are depicted with thin boundaries. Red areas indicate strong binding, while blue represents areas of weak binding.

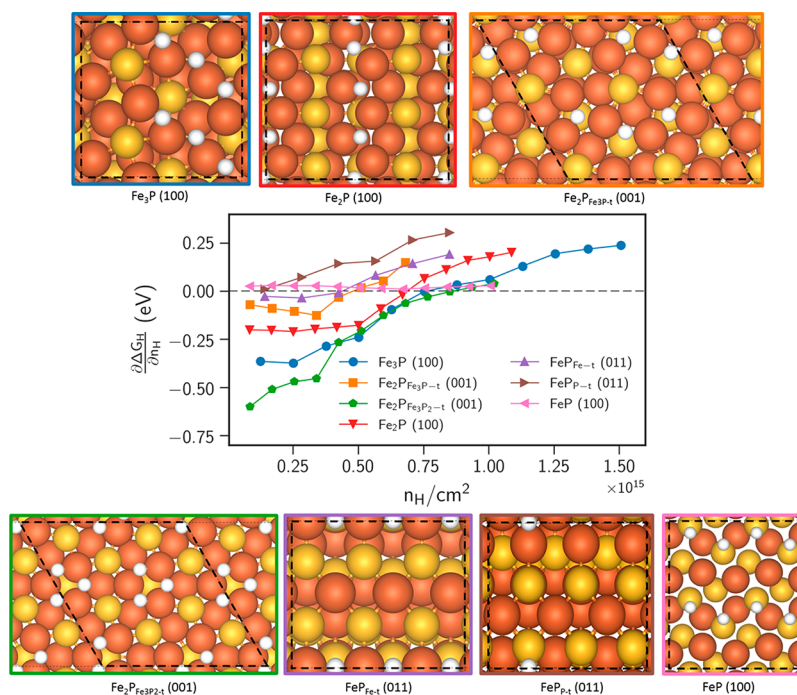


**Figure 7.** Coverage-dependent, differential Gibbs free binding energy for seven distinct  $\text{Fe}_x\text{P}$  models with different stoichiometries or terminations. The hydrogen adsorption geometries corresponding to the operating coverage nearest to thermoneutral binding are provided in the frame of the matching color.

Methods and Hydrogen Binding Contours), and the resulting contour maps of the hydrogen binding preferences for the  $\text{Fe}_3\text{P}$  (100),  $\text{Fe}_2\text{P}$  (100), and the Fe-terminated  $\text{FeP}_{\text{Fe-t}}$  (011) surfaces are given in Figure 6. Additional contour maps for  $\text{FeP}_{\text{P-t}}$  (011) and  $\text{FeP}$  (100) surfaces are given in Figure S33.

Analysis of binding preferences on representative  $\text{Fe}_3\text{P}$  (100) and  $\text{Fe}_2\text{P}$  (100) indicate that hydrogen generally prefers

binding to Fe-rich areas. Cleavage of  $\text{Fe}_3\text{P}$  along the (100) direction exposes a stepped surface, where hydrogen preferentially occupies the exposed Fe 3-fold or Fe–Fe bridge sites at low coverages. The bilayered (001) surface of  $\text{Fe}_2\text{P}$  consists of 3-fold Fe sites, while the (100) surface forms Fe bridge sites, which are again amenable to strong hydrogen binding. The  $\text{FeP}$  (011) surfaces exhibit weak hydrogen binding at the Fe–Fe and

Fe–P bridges on the Fe- and P-terminated surfaces, and overall, the weakest binding energies of all  $\text{Fe}_x\text{P}$  surfaces. Across all  $\text{Fe}_x\text{P}$  surfaces, the presence of a surface or subsurface P atom weakens hydrogen binding and is evidenced by the blue colored regions in Figure 6 and Figure S33. The low coverage adsorption geometries on  $\text{FeP}_{\text{P-t}}$  (011) reported in our work are contrary to those published by Kibsgaard and co-workers, who identified the active hydrogen atom to bind atop the  $\text{FeP}_{\text{P-t}}$  (011) surface P atoms. This surface was shown to be HER active under low coverages of 0.25 ML, with  $\Delta G_{\text{H}} = 0.13$  eV.<sup>53</sup> Assuming approximate entropic and zero point energy contributions of 0.25 eV to  $\Delta G_{\text{H}}$  in eq 2 (see Density Functional Theory Methods, SI),<sup>41,54</sup> hydrogen binds to P with an adsorption energy of  $-0.12$  eV. Our calculations show that hydrogen binds with a similar binding energy of  $-0.1$  eV at the Fe–P bridge sites, but even more favorable binding of  $-0.22$  eV is obtained for the Fe–Fe bridge site. We note that the computational setup used in this work is comparable to that used in the work of Kibsgaard and co-workers, but with a stricter force convergence criterion of 0.02 eV/Å. We speculate that the previously reported results might have been obtained by imposing artificial constraints on the hydrogen atom location for the purpose of consistency in comparing different catalysts and facets. The same  $\text{FeP}_{\text{P-t}}$  (011) surface was used in the work of Chung et al., who also reported results only for hydrogen bound atop the surface P atoms.<sup>54</sup>

The differential Gibbs free energy of hydrogen adsorption,  $\frac{\partial \Delta G_{\text{H}}}{\partial N_{\text{H}}}$ , at steady state coverage is widely accepted as a descriptor of HER activity on transition metals and transition metal phosphides.<sup>53,55–58</sup> This necessary, but not sufficient, condition requires that the  $\frac{\partial \Delta G_{\text{H}}}{\partial N_{\text{H}}}$  at the operating coverage be  $\sim 0$  eV, ensuring facile proton adsorption through the Volmer step and rapid recombination to evolve  $\text{H}_2$  through the Tafel or Heyrovsky steps.<sup>57</sup> Spontaneous adsorption and recombination of protons on the surface is conducive to high turnover rates, potentially resulting in excellent HER activity. Figure 7 charts the differential Gibbs free energy of hydrogen adsorption as a function of coverage in units of atoms ( $n_{\text{H}}$ ) per unit area ( $\text{cm}^2$ ) for all iron phosphide surfaces studied. Visualizations of all surface unit cells with steady state hydrogen coverage at the most thermoneutral differential  $\Delta G_{\text{H}}$  are also provided in Figure 7. Normalizing the number of hydrogens adsorbed per unit surface area provides for a meaningful metric that can be used to qualitatively and quantitatively compare models of different surface unit cell areas. All data used to generate Figure 7 are given in Tables S5–S13.

All considered iron phosphide surfaces reach the thermoneutral condition  $\frac{\partial \Delta G_{\text{H}}}{\partial N_{\text{H}}} \approx 0$  at some surface coverage, indicative of good HER performance. Moreover, most surfaces exhibit a reasonably flat dependence on hydrogen coverage near the thermoneutral value. The existence of a number of steps and kinks on most  $\text{Fe}_x\text{P}$  surfaces results in a largely accessible and flat potential energy surface for hydrogen adsorption. The exception to this trend is the  $\text{Fe}_2\text{P}$  (100) surface, which binds weakly through P-rich regions as hydrogen atoms are sequentially populated at HER active sites at higher coverages. Since all  $\text{Fe}_x\text{P}$  surfaces satisfy the necessary criterion of thermoneutral hydrogen adsorption, their activity differences may be attributed to different hydrogen surface coverages under reaction conditions. Invoking the law of mass action, the

rate of HER depends quadratically on the surface concentration of hydrogen. The lowest predicted hydrogen coverage is obtained for  $\text{FeP}_{\text{P-t}}$  (011), whereas the calculations show an ca. four times higher surface coverage on the  $\text{Fe}_2\text{P}$  and  $\text{Fe}_3\text{P}$  surfaces at the condition of thermoneutral hydrogen binding. Our consistently calculated hydrogen binding preferences across three distinct iron phosphide surfaces,  $\text{Fe}_3\text{P}$  (100),  $\text{Fe}_2\text{P}$  (100), and  $\text{FeP}$  (011), in Figure 6 is congruent with the interpretation that an increased P content on the FeP surface results in a lower hydrogen coverage and reduced HER activity can be expected. The lower number of active sites per unit surface area exhibited by FeP is again a direct consequence of the reduced availability of surface binding sites for H atoms, due to a higher stoichiometric concentration of P in FeP, compared to  $\text{Fe}_2\text{P}$  and  $\text{Fe}_3\text{P}$ .

Our simple analysis of various iron phosphide surfaces based on an accepted thermodynamic descriptor provides theoretical support for the observed HER activity of all three  $\text{Fe}_x\text{P}$  materials. Moreover, we propose that the higher hydrogen coverage for  $\text{Fe}_3\text{P}$  and  $\text{Fe}_2\text{P}$  under operating conditions is responsible for their better electrocatalytic performance compared to FeP, and we attribute the higher hydrogen coverage to the larger number of Fe rich sites on these surfaces. Our DFT calculations investigate the as-constructed  $\text{Fe}_x\text{P}$  surfaces for hydrogen binding and present HER activity trends for a particular surface relative to another. A more detailed analysis of these surfaces as HER catalysts would require determination of active surface terminations and surface reconstructions that may occur at reaction conditions similar to the work done by Rappe and co-workers.<sup>50,51</sup> Additional discrimination between the HER activity of  $\text{Fe}_3\text{P}$  and  $\text{Fe}_2\text{P}$  would also require the investigation of other important factors that govern the HER activity of a catalyst, such as the recombination kinetics or the electrical conductivity.<sup>51,59–61</sup>

## CONCLUSIONS

The single-source precursor MOCVD method employed for the deposition of the iron phosphides has permitted the formation of phase pure thin films of FeP and  $\text{Fe}_2\text{P}$  for the first time. The synthesis of these films enabled a systematic experimental and theoretical study of electrocatalytic activities of the iron phosphides in the series  $\text{Fe}_x\text{P}$  ( $x = 1–3$ ), which showed that their relative catalytic activity for the HER decreased with relative metal content in the order  $\text{Fe}_3\text{P} > \text{Fe}_2\text{P} > \text{FeP}$ . DFT investigations confirmed this trend with the primary conclusion that metal-rich phosphides  $\text{Fe}_3\text{P}$  and  $\text{Fe}_2\text{P}$  can support higher hydrogen coverages at thermoneutral hydrogen adsorption conditions, congruent with HER rates significantly higher than those of FeP being able to display under the same conditions.

Investigation of the formation of the  $\text{Fe}_x\text{P}$  phases ( $x = 1, 2$ ) showed that elimination of phosphine  $\text{Fe}(\text{CO})_4\text{L}$  ( $\text{L} = \text{PH}_3, \text{PH}_2^t\text{Bu}$ ) led to films that are metal-rich rather than possessing the stoichiometry of the SSP; however, this was overcome by varying the temperature of decomposition or altering the structure of the SSP so that the phosphorus ligands are more strongly bound to iron. The use of a precursor that contains a diphosphane unit also circumvented phosphine elimination and allowed for production of the films with the desired stoichiometry at comparatively lower temperatures.

Together, these results provide not only a route to production of phase-pure thin films of additional members of the iron phosphide family but also further our understanding of

the interplay between metal and phosphorus in TMP HER electrocatalysis. Additionally, that higher metal content is positively correlated with higher HER activity should influence future catalyst development, particularly of the  $M_3P$  phase, which will allow the practical realization of hydrogen production from water.

## ■ ASSOCIATED CONTENT

### 📄 Supporting Information

The Supporting Information is available free of charge on the ACS Publications website at DOI: [10.1021/acs.chemmater.8b01624](https://doi.org/10.1021/acs.chemmater.8b01624).

Experimental details for the synthesis of **3**, characterization and crystallographic data for **3** including  $^1H$  and  $^{31}P$  NMR spectra and ESI-MS spectra, film deposition parameters, experimental details for the detection of phosphine from the CVD decomposition of **1**, SEM images of the films, PXRD spectra of the films, electrochemical measurement details, and details of the DFT calculations (PDF)

Crystal Structure and Coordinates (CIF)

## ■ AUTHOR INFORMATION

### Corresponding Authors

\*E-mail: [whitmir@rice.edu](mailto:whitmir@rice.edu) (K.H. Whitmire).

\*E-mail: [jbao@uh.edu](mailto:jbao@uh.edu) (J. Bao).

\*E-mail: [grabow@uh.edu](mailto:grabow@uh.edu) (L. C. Grabow).

### ORCID

Lars C. Grabow: 0000-0002-7766-8856

Jiming Bao: 0000-0002-6819-0117

Kenton H. Whitmire: 0000-0001-7362-535X

### Author Contributions

<sup>†</sup>These authors contributed equally (D.E. Schipper and Z. Zhao).

### Notes

The authors declare no competing financial interest.

## ■ ACKNOWLEDGMENTS

George C. Sheldrick, University of Göttingen, is acknowledged for help with the crystal structure of **3**. The authors thank Rice University, the National Science Foundation (CHE-1411495, K.H.W.), and the Robert A. Welch Foundation (C-0976, K.H.W.; E-1728, J.B.) for funding. This material is based upon work supported by the National Science Foundation Graduate Research Fellowship (D.E.S.) under Grant No. 1450681. H.T. and L.C.G. acknowledge financial support from NSF-CBET 1605331 and NSF CAREER Award No. 1454384, respectively. Computational resources were provided by the uHPC cluster managed by the University of Houston and acquired through NSF-MRI Award No. 1531814. This work used the Extreme Science and Engineering Discovery Environment (XSEDE), which is supported by National Science Foundation Grant No. ACI-1053575. We also acknowledge the use of computational resources provided by the National Energy Research Scientific Computing (NERSC) Center, a DOE Office of Science User Facility supported by the Office of Science of the U.S. Department of Energy under Contract No. DE-AC02-05CH11231. Finally, we thank the Center of Advanced Computing and Data Systems (CACDS) and the Research Computing Center (RCC) at the University of Houston for access to the Maxwell/Opuntia/Sabine HPC clusters.

## ■ REFERENCES

- (1) Chen, J.-H.; Whitmire, K. H. A Structural Survey of the Binary Transition Metal Phosphides and Arsenides of the d-Block Elements. *Coord. Chem. Rev.* **2018**, *355*, 271–327.
- (2) Okamoto, H. The Fe-P (Iron-Phosphorus) System. *Bull. Alloy Phase Diagrams* **1990**, *11*, 404–412.
- (3) Lisher, E. J.; Wilkinson, C.; Ericsson, T.; Haggstrom, L.; Lundgren, L.; Wappling, R. Studies of the Magnetic Structure of  $Fe_3P$ . *J. Phys. C: Solid State Phys.* **1974**, *7*, 1344–1352.
- (4) Fiechter, S.; Tributsch, H.; Evain, M.; Brec, R.  $\gamma-FeP_4$ , a New Photosensitive Semiconductor. *Mater. Res. Bull.* **1987**, *22*, 543–549.
- (5) Caron, L.; Hudl, M.; Högl, V.; Dung, N. H.; Gomez, C. P.; Sahlberg, M.; Brück, E.; Andersson, Y.; Nordblad, P. Magnetocrystalline Anisotropy and the Magnetocaloric Effect in  $Fe_2P$ . *Phys. Rev. B: Condens. Matter Mater. Phys.* **2013**, *88*, 094440.
- (6) Tegus, O.; Brück, E.; Buschow, K. H. J.; de Boer, F. R. Transition-Metal-Based Magnetic Refrigerants for Room-Temperature Applications. *Nature* **2002**, *415*, 150–152.
- (7) Hall, J. W.; Membreno, N.; Wu, J.; Celio, H.; Jones, R. A.; Stevenson, K. J. Low-Temperature Synthesis of Amorphous  $FeP_2$  and Its Use as Anodes for Li Ion Batteries. *J. Am. Chem. Soc.* **2012**, *134*, 5532–5535.
- (8) Boyanov, S.; Bernardi, J.; Gillot, F.; Dupont, L.; Womes, M.; Tarascon, J.-M.; Monconduit, L.; Doublet, M.-L.  $FeP$ : Another Attractive Anode for the Li-Ion Battery Enlisting a Reversible Two-Step Insertion/Conversion Process. *Chem. Mater.* **2006**, *18*, 3531–3538.
- (9) Oyama, S. T. Novel Catalysts for Advanced Hydroprocessing: Transition Metal Phosphides. *J. Catal.* **2003**, *216*, 343–352.
- (10) Xu, Y.; Wu, R.; Zhang, J.; Shi, Y.; Zhang, B. Anion-Exchange Synthesis of Nanoporous  $FeP$  Nanosheets as Electrocatalysts for Hydrogen Evolution Reaction. *Chem. Commun.* **2013**, *49*, 6656–6658.
- (11) Callejas, J. F.; McEnaney, J. M.; Read, C. G.; Crompton, J. C.; Biacchi, A. J.; Popczun, E. J.; Gordon, T. R.; Lewis, N. S.; Schaak, R. E. Electrocatalytic and Photocatalytic Hydrogen Production from Acidic and Neutral-pH Aqueous Solutions Using Iron Phosphide Nanoparticles. *ACS Nano* **2014**, *8*, 11101–11107.
- (12) Li, D.; Baydoun, H.; Verani, C. N.; Brock, S. L. Efficient Water Oxidation Using  $CoMnP$  Nanoparticles. *J. Am. Chem. Soc.* **2016**, *138*, 4006–4009.
- (13) Dutta, A.; Samantara, A. K.; Dutta, S. K.; Jena, B. K.; Pradhan, N. Surface-Oxidized Dicobalt Phosphide Nanoneedles as a Nonprecious, Durable, and Efficient OER Catalyst. *ACS Energy Lett.* **2016**, *1*, 169–174.
- (14) Deng, C.; Xie, J.; Xue, Y.; He, M.; Wei, X.; Yan, Y.-M. Synthesis of  $MoP$  Decorated Carbon Cloth as a Binder-Free Electrode for Hydrogen Evolution. *RSC Adv.* **2016**, *6*, 68568–68573.
- (15) McEnaney, J. M.; Crompton, J. C.; Callejas, J. F.; Popczun, E. J.; Read, C. G.; Lewis, N. S.; Schaak, R. E. Electrocatalytic Hydrogen Evolution Using Amorphous Tungsten Phosphide Nanoparticles. *Chem. Commun.* **2014**, *50*, 11026–11028.
- (16) Kibsgaard, J.; Tsai, C.; Chan, K.; Benck, J. D.; Nørskov, J. K.; Abild-Pedersen, F.; Jaramillo, T. F. Designing an Improved Transition Metal Phosphide Catalyst for Hydrogen Evolution Using Experimental and Theoretical Trends. *Energy Environ. Sci.* **2015**, *8*, 3022–3029.
- (17) Li, D.; Baydoun, H.; Kulikowski, B.; Brock, S. L. Boosting the Catalytic Performance of Iron Phosphide Nanorods for the Oxygen Evolution Reaction by Incorporation of Manganese. *Chem. Mater.* **2017**, *29*, 3048–3054.
- (18) Zhang, Y.; Zhang, H.; Feng, Y.; Liu, L.; Wang, Y. Unique  $Fe_2P$  Nanoparticles Enveloped in Sandwichlike Graphited Carbon Sheets as Excellent Hydrogen Evolution Reaction Catalyst and Lithium-Ion Battery Anode. *ACS Appl. Mater. Interfaces* **2015**, *7*, 26684–26690.
- (19) Xiao, P.; Chen, W.; Wang, X. A Review of Phosphide-Based Materials for Electrocatalytic Hydrogen Evolution. *Adv. Energy Mater.* **2015**, *5*, 1500985.
- (20) Leitner, A. P.; Chen, J.-H.; Schipper, D. E.; Whitmire, K. H. Thin Films of  $(Fe_{1-x}Co_x)_3P$  and  $Fe_3(P_{1-x}Te_x)$  from the Co-

Decomposition of Organometallic Precursors by MOCVD. *Chem. Mater.* **2016**, *28*, 7066–7071.

(21) Colson, A. C.; Chen, C.-W.; Morosan, E.; Whitmire, K. H. Synthesis of Phase-Pure Ferromagnetic Fe<sub>3</sub>P Films from Single-Source Molecular Precursors. *Adv. Funct. Mater.* **2012**, *22*, 1850–1855.

(22) Leitner, A. P.; Schipper, D. E.; Chen, J.-H.; Colson, A. C.; Rusakova, I.; Rai, B. K.; Morosan, E.; Whitmire, K. H. Synthesis of Hexagonal FeMnP Thin Films from a Single-Source Molecular Precursor. *Chem. - Eur. J.* **2017**, *23*, 5565–5572.

(23) Schipper, D. E.; Zhao, Z.; Leitner, A. P.; Xie, L.; Qin, F.; Alam, M. K.; Chen, S.; Wang, D.; Ren, Z.; Wang, Z.; Bao, J.; Whitmire, K. H. A TiO<sub>2</sub>/FeMnP Core/Shell Nanorod Array Photoanode for Efficient Photoelectrochemical Oxygen Evolution. *ACS Nano* **2017**, *11*, 4051–4059.

(24) Hunger, C.; Ojo, W.-S.; Bauer, S.; Xu, S.; Zabel, M.; Chaudret, B.; Lacroix, L.-M.; Scheer, M.; Nayral, C.; Delpech, F. Stoichiometry-Controlled FeP Nanoparticles Synthesized from a Single Source Precursor. *Chem. Commun.* **2013**, *49*, 11788–11790.

(25) Dias, P. B.; de Piedade, M. E. M.; Simões, J. A. M. Bonding and Energetics of Phosphorus (III) Ligands in Transition Metal Complexes. *Coord. Chem. Rev.* **1994**, *135*, 737–807.

(26) Jones, P. G.; Roesky, H. W.; Grützmacher, H.; Sheldrick, G. M. Oxidative Knüpfung Einer Phosphor-Phosphor-Bindung Unter Einwirkung von Ag(I)- Bzw. Cu(II)-Ionen: Synthese Und Struktur von [(C<sub>6</sub>H<sub>5</sub>)PH<sub>2</sub>Ag{μ-(C<sub>6</sub>H<sub>5</sub>PH)<sub>2</sub>}]<sub>2</sub>(AsF<sub>6</sub>)<sub>2</sub>, Einem Sechsgliedrigen Silber-Phosphor-Ring/The Oxidative Formation of a Phosphorus-Phosphorus Bond in the Presence of Ag(I) and Cu(II) Ions: Synthesis and Structure of [(C<sub>6</sub>H<sub>5</sub>)PH<sub>2</sub>Ag{μ-(C<sub>6</sub>H<sub>5</sub>PH)<sub>2</sub>}]<sub>2</sub>(AsF<sub>6</sub>)<sub>2</sub>, Containing a Six-Membered Silver-Phosphorus Ring. *Z. Naturforsch., B: J. Chem. Sci.* **1985**, *40*, 590–593.

(27) Duffy, M. P.; Ting, L. Y.; Nicholls, L.; Li, Y.; Ganguly, R.; Mathey, F. Reaction of Terminal Phosphinidene Complexes with Dihydrogen. *Organometallics* **2012**, *31*, 2936–2939.

(28) Tian, R.; Mei, Y.; Duan, Z.; Mathey, F. Simple Access to Tungsten-Stabilized Disubstituted Diphosphines. *Organometallics* **2013**, *32*, 5615–5618.

(29) Barlett, R. A.; Dias, H. V. R.; Flynn, K. M.; Hope, H.; Murray, B. D.; Olmstead, M. M.; Power, P. P. Reaction of Bulky Monosubstituted Phosphorus(III) Halides with Disodium Pentacarbonylchromate. Steric and Electronic Factors in the Synthesis of Cr(CO)<sub>5</sub> Complexes of Diphosphenes, Phosphinidenes, Phosphanes, Diphosphanes, and Cyclopolyphosphanes. *J. Am. Chem. Soc.* **1987**, *109*, 5693–5698.

(30) Huttner, G.; Müller, H.-D.; Bejenke, V.; Orama, O. Die Struktur von Bis(Cyclopentadienyldicarbonylmangan)-1,2-Diphenyldiphosphan, [C<sub>5</sub>H<sub>5</sub>(CO)<sub>2</sub>Mn]<sub>2</sub>PhP(H)–(H)PPh. *Z. Naturforsch., B: J. Chem. Sci.* **1976**, *31*, 1166–1169.

(31) Schubert, E. H.; Sheline, R. K. The Photochemical Synthesis of Pentacarbonyliron(0) Derivatives. *Inorg. Chem.* **1966**, *5*, 1071–1074.

(32) Weiss, E.; Stark, K.; Lancaster, J. E.; Murdoch, H. D. π-Olefin-Eisentetracarbonyl-Komplexe Mit Liganden Der Malein-, Fumar-, Acryl-, Methacryl- Und Zimtsäure-Reihe. *Helv. Chim. Acta* **1963**, *46*, 288–297.

(33) Blanchard, P. E. R.; Grosvenor, A. P.; Cavell, R. G.; Mar, A. X-Ray Photoelectron and Absorption Spectroscopy of Metal-Rich Phosphides M<sub>2</sub>P and M<sub>3</sub>P (M = Cr–Ni). *Chem. Mater.* **2008**, *20*, 7081–7088.

(34) Pinaud, B. A.; Benck, J. D.; Seitz, L. C.; Forman, A. J.; Chen, Z.; Deutsch, T. G.; James, B. D.; Baum, K. N.; Baum, G. N.; Ardo, S.; Wang, H.; Miller, E.; Jaramillo, T. J. Technical and Economic Feasibility of Centralized Facilities for Solar Hydrogen Production via Photocatalysis and Photoelectrochemistry. *Energy Environ. Sci.* **2013**, *6*, 1983–2002.

(35) Xie, J.; Zhang, H.; Li, S.; Wang, R.; Sun, X.; Zhou, M.; Zhou, J.; Lou, X. W. D.; Xie, Y. Defect-Rich MoS<sub>2</sub> Ultrathin Nanosheets with Additional Active Edge Sites for Enhanced Electrocatalytic Hydrogen Evolution. *Adv. Mater.* **2013**, *25*, 5807–5813.

(36) Shi, Y.; Zhang, B. Recent Advances in Transition Metal Phosphide Nanomaterials: Synthesis and Applications in Hydrogen Evolution Reaction. *Chem. Soc. Rev.* **2016**, *45*, 1529–1541.

(37) Merki, D.; Vrabel, H.; Rovelli, L.; Fierro, S.; Hu, X. Fe, Co, and Ni Ions Promote the Catalytic Activity of Amorphous Molybdenum Sulfide Films for Hydrogen Evolution. *Chem. Sci.* **2012**, *3*, 2515–2525.

(38) Zhou, W.; Jia, J.; Lu, J.; Yang, L.; Hou, D.; Li, G.; Chen, S. Recent Developments of Carbon-Based Electrocatalysts for Hydrogen Evolution Reaction. *Nano Energy* **2016**, *28*, 29–43.

(39) Durst, J.; Siebel, A.; Simon, C.; Hasché, F.; Herranz, J.; Gasteiger, H. A. New Insights into the Electrochemical Hydrogen Oxidation and Evolution Reaction Mechanism. *Energy Environ. Sci.* **2014**, *7*, 2255–2260.

(40) Chen, R.; Yang, C.; Cai, W.; Wang, H.-Y.; Miao, J.; Zhang, L.; Chen, S.; Liu, B. Use of Platinum as the Counter Electrode to Study the Activity of Nonprecious Metal Catalysts for the Hydrogen Evolution Reaction. *ACS Energy Lett.* **2017**, *2*, 1070–1075.

(41) Zhao, Z.; Qin, F.; Kasiraju, S.; Xie, L.; Alam, M. K.; Chen, S.; Wang, D.; Ren, Z.; Wang, Z.; Grabow, L. C.; Bao, J. Vertically Aligned MoS<sub>2</sub>/Mo<sub>2</sub>C Hybrid Nanosheets Grown on Carbon Paper for Efficient Electrocatalytic Hydrogen Evolution. *ACS Catal.* **2017**, *7*, 7312–7318.

(42) Zhao, Z.; Schipper, D. E.; Leitner, A. P.; Thirumalai, H.; Chen, J.-H.; Xie, L.; Qin, F.; Alam, M. K.; Grabow, L. C.; Chen, S.; Wang, D.; Ren, Z.; Wang, Z.; Whitmire, K. H.; Bao, J. Bifunctional Metal Phosphide FeMnP Films from Single Source Metal Organic Chemical Vapor Deposition for Efficient Overall Water Splitting. *Nano Energy* **2017**, *39*, 444–453.

(43) Lv, C.; Peng, Z.; Zhao, Y.; Huang, Z.; Zhang, C. The Hierarchical Nanowires Array of Iron Phosphide Integrated on a Carbon Fiber Paper as an Effective Electrocatalyst for Hydrogen Generation. *J. Mater. Chem. A* **2016**, *4*, 1454–1460.

(44) Yan, Y.; Xia, B. Y.; Ge, X.; Liu, Z.; Fisher, A.; Wang, X. A Flexible Electrode Based on Iron Phosphide Nanotubes for Overall Water Splitting. *Chem. - Eur. J.* **2015**, *21*, 18062–18067.

(45) Yan, Y.; Thia, L.; Xia, B. Y.; Ge, X.; Liu, Z.; Fisher, A.; Wang, X. Construction of Efficient 3D Gas Evolution Electrocatalyst for Hydrogen Evolution: Porous FeP Nanowire Arrays on Graphene Sheets. *Adv. Sci.* **2015**, *2*, 1500120.

(46) Tian, L.; Yan, X.; Chen, X. Electrochemical Activity of Iron Phosphide Nanoparticles in Hydrogen Evolution Reaction. *ACS Catal.* **2016**, *6*, 5441–5448.

(47) Son, C. Y.; Kwak, I. H.; Lim, Y. R.; Park, J. FeP and FeP<sub>2</sub> Nanowires for Efficient Electrocatalytic Hydrogen Evolution Reaction. *Chem. Commun.* **2016**, *52*, 2819–2822.

(48) Liu, M.; Yang, L.; Liu, T.; Tang, Y.; Luo, S.; Liu, C.; Zeng, Y. Fe<sub>2</sub>P/Reduced Graphene Oxide/Fe<sub>2</sub>P Sandwich-Structured Nanowall Arrays: A High-Performance Non-Noble-Metal Electrocatalyst for Hydrogen Evolution. *J. Mater. Chem. A* **2017**, *5*, 8608–8615.

(49) Read, C. G.; Callejas, J. F.; Holder, C. F.; Schaak, R. E. General Strategy for the Synthesis of Transition Metal Phosphide Films for Electrocatalytic Hydrogen and Oxygen Evolution. *ACS Appl. Mater. Interfaces* **2016**, *8*, 12798–12803.

(50) Laursen, A. B.; Wexler, R. B.; Whitaker, M. J.; Izett, E. J.; Calvino, K. U. D.; Hwang, S.; Rucker, R.; Wang, H.; Li, J.; Garfunkel, E.; Greenblatt, M.; Rappe, A. M.; Dismukes, G. C. Climbing the Volcano of Electrocatalytic Activity While Avoiding Catalyst Corrosion: Ni<sub>3</sub>P, a Hydrogen Evolution Electrocatalyst Stable in Both Acid and Alkali. *ACS Catal.* **2018**, *8*, 4408–4419.

(51) Wexler, R. B.; Martinez, J. M. P.; Rappe, A. M. Active Role of Phosphorus in the Hydrogen Evolving Activity of Nickel Phosphide (0001) Surfaces. *ACS Catal.* **2017**, *7*, 7718–7725.

(52) Docherty, R.; Clydesdale, G.; Roberts, K. J.; Bennema, P. Application of Bravais-Friedel-Donnay-Harker, Attachment Energy and Ising Models to Predicting and Understanding the Morphology of Molecular Crystals. *J. Phys. D: Appl. Phys.* **1991**, *24*, 89–99.

(53) Kibsgaard, J.; Tsai, C.; Chan, K.; Benck, J. D.; Nørskov, J. K.; Abild-Pedersen, F.; Jaramillo, T. F. Designing an Improved Transition Metal Phosphide Catalyst for Hydrogen Evolution Using Experimental and Theoretical Trends. *Energy Environ. Sci.* **2015**, *8*, 3022–3029.

(54) Chung, D. Y.; Jun, S. W.; Yoon, G.; Kim, H.; Yoo, J. M.; Lee, K. S.; Kim, T.; Shin, H.; Sinha, A. K.; Kwon, S. G.; Kang, K.; Hyeon, T.;

Sung, Y.-E. Large-Scale Synthesis of Carbon-Shell-Coated FeP Nanoparticles for Robust Hydrogen Evolution Reaction Electrocatalyst. *J. Am. Chem. Soc.* **2017**, *139*, 6669–6674.

(55) Nørskov, J. K.; Bligaard, T.; Logadottir, A.; Kitchin, J. R.; Chen, J. G.; Pandelov, S.; Stimming, U. Trends in the Exchange Current for Hydrogen Evolution. *J. Electrochem. Soc.* **2005**, *152*, J23–J26.

(56) Seh, Z. W.; Kibsgaard, J.; Dickens, C. F.; Chorkendorff, I.; Nørskov, J. K.; Jaramillo, T. F. Combining Theory and Experiment in Electrocatalysis: Insights into Materials Design. *Science* **2017**, *355*, eaad4998.

(57) Skúlason, E.; Karlberg, G. S.; Rossmeisl, J.; Bligaard, T.; Greeley, J.; Jónsson, H.; Nørskov, J. K. Density Functional Theory Calculations for the Hydrogen Evolution Reaction in an Electrochemical Double Layer on the Pt(111) Electrode. *Phys. Chem. Chem. Phys.* **2007**, *9*, 3241–3250.

(58) Greeley, J.; Nørskov, J. K.; Kibler, L. A.; El-Aziz, A. M.; Kolb, D. M. Hydrogen Evolution over Bimetallic Systems: Understanding the Trends. *ChemPhysChem* **2006**, *7*, 1032–1035.

(59) Kucernak, A. R. J.; Naranammalpuram Sundaram, V. N. Nickel Phosphide: The Effect of Phosphorus Content on Hydrogen Evolution Activity and Corrosion Resistance in Acidic Medium. *J. Mater. Chem. A* **2014**, *2*, 17435–17445.

(60) Jaramillo, T. F.; Jørgensen, K. P.; Bonde, J.; Nielsen, J. H.; Horch, S.; Chorkendorff, I. Identification of Active Edge Sites for Electrochemical H<sub>2</sub> Evolution from MoS<sub>2</sub> Nanocatalysts. *Science* **2007**, *317*, 100–102.

(61) Liao, L.; Zhu, J.; Bian, X.; Zhu, L.; Scanlon, M. D.; Girault, H. H.; Liu, B. MoS<sub>2</sub> Formed on Mesoporous Graphene as a Highly Active Catalyst for Hydrogen Evolution. *Adv. Funct. Mater.* **2013**, *23*, 5326–5333.